

1 Spatio-Temporal Entropy Analysis Of The Magnetic 2 Field To Help Magnetic Cloud Characterization

Ojeda, G. A.,^{1,2} Mendes, O. ,¹ Calzadilla M. A,² and Domingues, M. O.³

Arian Ojeda González, Divisão de Geofísica Espacial-DGE, Coordenação Geral de Ciências Espaciais e Atmosféricas - CEA, Instituto Nacional de Pesquisas Espaciais - INPE, Av. dos Astronautas, 1.758 - Jd. Granja - São José dos Campos - SP - Brasil - CEP 12227-010. (arian@dge.inpe.br)

Odim Mendes Junior, Divisão de Geofísica Espacial-DGE, Coordenação Geral de Ciências Espaciais e Atmosféricas - CEA, Instituto Nacional de Pesquisas Espaciais - INPE, Av. dos Astronautas, 1.758 - Jd. Granja - São José dos Campos - SP - Brasil - CEP 12227-010.

Alexander Calzadilla Méndez, Departamento de Geofísica Espacial, Instituto de Geofísica y Astronomía - IGA, calle 212, 2906 e/ 29 y 31, La Coronela - La Lisa - Ciudad de la Habana - CUBA CP 11600.

Margarete Domingues Oliveira, Laboratório Associado de Computação e Matemática Aplicada, Coordenação de Laboratórios associados- CTE, Instituto Nacional de Pesquisas Espaciais - INPE, Av. dos Astronautas, 1.758 - Jd. Granja - São José dos Campos - SP - Brasil - CEP 12227-010.

¹DGE/CEA/National Institute for Space

3 Abstract.

4 The aim of this work is to create a methodology to characterize the dy-
5 namics of magnetic clouds (MCs) from signals measured by satellites in the
6 interplanetary medium. We have tested Spatio-Temporal Entropy (STE) tech-
7 nique to study 41 MCs identified by other authors, where the plasma sheath
8 region has been identified. The STE was implemented in Visual Recurrence
9 Analysis (VRA) software to quantify the order in the recurrence plot. Some
10 tests using synthetic time series were performed to validate the method. In
11 particular, we worked with IMF components B_x , B_y , B_z of 16 s. Time win-
12 dows from March 1998 to December 2003 for some MCs were selected. We
13 found higher STE values in the sheaths and zero STE values in some of the
14 three components in most of the MCs (30 among 41 events). The trend is
15 the principal cause of the lower STE values in the MCs. Also, MCs have mag-

Research - INPE 12227-010 São José dos

Campos, SP, Brazil.

²Department of Space Geophysics,

Institute of Geophysics and Astronomy -

IGA Havana City, Cuba.

³LAC/CTE/National Institute for Space

Research - INPE 12227-010 São José dos

Campos, SP, Brazil.

16 netic field more structured than sheath and quiet solar wind. We have done
17 a test considering the magnetic components of a cylindrically symmetric force-
18 free constructed analytically, with the result of zero STE value. It agrees with
19 the physical assumption of finding zero STE values when studying experi-
20 mental data in MC periods. The new feature just examined here adds to the
21 usual features, as described in Burlaga et al. [1981], for the characterization
22 of MCs. The STE calculation can be an auxiliary objective tool to identify
23 flux-ropes associated with MCs, mainly during events with no available plasma
24 data but only with IMF.

1. Introduction

25 The term magnetic cloud (MC) has been used to characterize an Interplanetary Coronal
26 Mass Ejection (ICME) that presents a specific configuration, in which the magnetic field
27 strength is [higher than average IMF](#), the magnetic field direction rotates smoothly through
28 a large angle, and the proton temperature is low [Burlaga et al., 1981; Klein and Burlaga,
29 1982; Gosling, 1990]. Typically a flux-rope ejected from the Sun described the magnetic
30 configuration of a MC. The MCs are observed in a clear way when the spacecraft crosses
31 the magnetic field structure close by its center [Schwenn, 2006]. *In-situ* measurements are
32 limited to the spacecraft trajectory crossing the incoming ICME. Therefore, one needs
33 to rely on modeling evaluation in order to derive the global magnetic structure from
34 available local measurements [Démoulin and Dasso, 2009]. [Due to MCs moving faster](#)
35 [than the surrounding solar wind \(SW\), plasmas and magnetic field typically accumulate](#)
36 [in front of it, creating a preceding disturbed sheath.](#)

37 In Ojeda et al. [2005], a study considering 20 MCs, 17 [non-MC ICMEs](#), and 20 time
38 series of equivalent time duration of quiet SW was done. The IMF B_z and solar wind V_x
39 components in a time interval of 48 h before each MC were analyzed. Under MC con-
40 ditions, a feature was identified that the component B_z of the IMF has the tendency to
41 present lower spatio-temporal entropy (name given by Eugene Kononov's Visual Recur-
42 rence Analysis (VRA) software, not to be confused with spatio-temporal entropy image
43 (STEI) [Ma and Zhang, 2001]) values than the B_z in other cases, such as in [non-MC](#)
44 [ICMEs](#) and during quiet SW. This behavior seems to be very interesting under a physical
45 point of view. Thus in this work a more detailed study of the spatio-temporal entropy

46 (STE) in MCs is carried out. The analyses are expanded to study the three magnetic
 47 components (B_x , B_y and B_z) using more complete dataset. The aim of this work is to
 48 validate the STE calculation technique as an useful tool to identify features of the MCs.
 49 A proposed approach to study the MCs by analyzing the time series of interplanetary
 50 magnetic field (IMF) is presented.

51 The content is organized as follows. In Section 2, a review on the theoretical and obser-
 52 vational aspects of the interplanetary MCs is presented. In Section 3, the dataset used is
 53 described. In Section 4, a STE methodology for analyses is established. In Section 5, we
 54 compare STE values for time series corresponding to the MCs and the sheaths identified
 55 by Huttunen et al. [2005]. Finally, in Section 6 the conclusions are done. In Appendices,
 56 information on the tool is presented. Appendix A, shows a review on the tool in the VRA
 57 software. And Appendix B, the methods for calculating the entropy in the recurrence
 58 plot.

2. Magnetic Clouds

59 The pioneer studies on plasma clouds emitted by the Sun were developed about
 60 1950s [Morrison, 1954; Cocconi et al., 1958; Piddington, 1958]. However the definition
 61 and the term of "magnetic cloud" were presented by the first time in the work of Burlaga
 62 et al. [1981]. Nowadays the specific signatures which have to be necessarily fulfilled are
 63 the following: (1) smooth rotation in \vec{B} with low variance; (2) low proton temperature
 64 and (3) low plasma β , which is the ratio of the plasma pressure, $p = nk_B T$, to the mag-
 65 netic pressure, $p_{mag} = B^2/2\mu_0$ where n is number density, K_B Boltzmann constant, T
 66 temperature, B magnetic field and μ_0 magnetic permeability of the free space.

67 Initial studies to analyze the three-dimensional configuration of the magnetic field of
68 these [phenomenon have been](#) developed by Burlaga et al. [1981]. The minimum variance
69 analysis (MVA) was used as a method to identify and describe planar magnetic field
70 configuration associated with thin current sheets in the SW [Burlaga and Klein, 1980]
71 and planetary magnetospheres [Lepping and Behannon, 1979]. Burlaga et al. [1981] used
72 MVA to analyze the magnetic field configuration in a MC observed with 4 spacecraft:
73 Voyager 1 and 2, IMP 8, and Helios 2. They concluded that MC could be represented
74 as a magnetic cylinder whose axis lies close in the equatorial plane, marking an angle of
75 nearly 90° with respect to the radial direction.

76 Considering a cylindrical geometry for MCs, the MVA [Sonnerup and Cahill, 1967] re-
77 sulted an useful tool to calculate the direction of the cloud axis. Klein and Burlaga [1982]
78 identified 45 events in the period between 1967 and 1978, where the latitude and longitude
79 of the clouds axis were calculated. The results of Burlaga et al. [1981] also were consistent
80 with other configurations. Ivanov and Harshiladze [1984] created a mathematical formula-
81 tion using a cloud configuration as an oblate ellipsoidal. To understand how the magnetic
82 field configuration evolves in the SW may be necessary for the correct interpretation of
83 the field structure in MC [Burlaga and Behannon, 1982].

84 Goldstein [1983] considered a force-free configuration in the search for a stable topology
85 of the MCs. Marubashi [1986] studied interplanetary magnetic field data from the Pio-
86 neer Venus orbiter (PVO) between December 1978 to May 1984 in search of interplanetary
87 magnetic flux ropes near the Venus orbit. As a result, twenty-six well defined flux ropes
88 were found which have characteristics similar to those of flux ropes observed near Earth.
89 In one case, where the Sun, Venus and Earth were closely aligned, an almost identical

90 structure was observed by the PVO and the Earth-orbiting spacecraft with a time delay
91 of about 36 hours. This observation provides evidence that the structure of interplanetary
92 magnetic flux ropes are maintained during propagation at least from 0.72 AU (Astronom-
93 ical Unit (AU): The average distance from the Earth to the Sun. One AU = 93 million
94 miles or 149.6 million km) to 1 AU. A simple solution for a cylindrically symmetric
95 force-free field with constant alpha was studied by Lundquist [1950], and mentioned also
96 in Lundquist [1951]. Burlaga [1988] studied the above solution with constant alpha to
97 describe the types of signatures observed in the SW at 1 AU when MCs move past a
98 spacecraft.

99 In order to find plasma beta values significantly lower than one to identify MCs, space-
100 craft measurements of magnetic field and plasma are required. Sometimes the temperature
101 and density data on spacecraft have many gaps during periods in which the plasma in-
102 struments are saturated as a result of intense particle fluxes (for example, Bastille Day in
103 the ACE spacecraft). If this condition occurs, it makes impossible to calculate the plasma
104 beta, but it is still possible to detect the MC using magnetometers data [e.g., Huttunen
105 et al., 2005; Nieves-Chinchilla et al., 2005]. Here is the contribution we intend to do with
106 this work, showing an approach that could help to identify MCs, and it is proposed as
107 basis for an auxiliary analysis tool.

108 The main contributions related to the identification of MCs are summarized in Table 1.
109 It was adapted from Huttunen et al. [2005] and updated by us. We show in each column
110 of this table, the paper, the period of the investigation, the examination period (T_t),
111 the spacecraft used (Spacf), and the quantities number of MCs identified. Bothmer and
112 Rust [1997]; Bothmer and Schwenn [1998]; Huttunen et al. [2005] identified MCs based

113 on the MVA method; Mulligan et al. [1998] identified and classified MCs using the visual
 114 inspection of the data; Lynch et al. [2003] and Wu et al. [2003, /WIND list] used the least-
 115 square fitting routine by Lepping et al. [1990]; while Nieves-Chinchilla et al. [2005] studied
 116 all the MCs observed during the time interval 2000 – 2003 using the elliptical cross-section
 117 model [Hidalgo, 2003, 2005], where a distortion and expansion of the cross-section of the
 118 cloud is included from first principles.

119 From 1997 – 2003 in solar cycle 23, SW data were investigated by Huttunen et al.
 120 [2005] using the MVA method [Sonnerup and Cahill, 1967; Bothmer and Schwenn, 1998]
 121 to determine if they have flux-rope structures. They identified 73 MCs observed by the
 122 ACE and WIND spacecraft. In principle the axis of a MC can have any orientation
 123 with respect to the ecliptic plane [Bothmer and Schwenn, 1994, 1998], identified by the
 124 azimuthal direction in the ecliptic, called ϕ_C , and the inclination relative to the ecliptic,
 125 called θ_C . With the MVA, the angles above can be calculated [Bothmer and Schwenn,
 126 1998]. In order to classify MCs [Huttunen et al., 2005, and references therein], eight flux
 127 rope categories are often used, clustered as: Bipolar MCs (low inclination, and flux rope-
 128 type: SWN, SEN, NES, NWS), $\theta_C \leq 45^\circ$ and Unipolar MCs (high inclination, and flux
 129 rope-type: WNE, ESW, ENW, WSE), $\theta_C > 45^\circ$, where the meanings are S for south, N
 130 North, W west and E east.

131 Huttunen and collaborators have also included seven cloud candidate events for which
 132 either the fitting with MVA was not successful (e.g. the eigenvalue ratio < 2 or the
 133 directional change less than 30°) or there were large values of beta throughout the event.
 134 In their study, [the criterion to identify a MC was based on the smoothness of the rotation](#)
 135 [in the magnetic field direction confined to one plane. Additionally they required that a](#)

136 MC must have the average values of the plasma beta less than 0.5, the maximum value
137 of the magnetic field at least 8 nT, and the duration at least 6 h. The last two criteria
138 have been created with the objective of exclude “small and weak MCs”. All selected
139 events were investigated by analyzing 1 h magnetic field data with the minimum variance
140 analysis (MVA), where MCs are identified from the smooth rotation of the magnetic field
141 vector in the plane of the maximum variance [Klein and Burlaga, 1982]. For MCs with
142 durations of 12 h or less Huttunen et al. [2005] performed MVA using 5-min (WIND) or
143 4-min (ACE) averaged data.

3. IMF Dataset

144 The IMF dataset used in this work are measurements obtained by the ACE satellite.
145 The ACE spacecraft is in orbit around $L1$ from 1997 [Smith et al., 1998]. Where the
146 Lagrangean point $L1$ is a gravitational equilibrium point between the Sun and Earth at
147 about 1.5 million km from Earth and 148.5 million km from the Sun. On board of ACE a
148 total of ten instruments, was launched toward $L1$ [McComas et al., 1998], but in this work
149 only the Magnetic Field Experiment (MAG) is used. The MAG on board ACE consists
150 of twin vector fluxgate magnetometers to measure the IMF [Smith et al., 1998]. The data
151 (<http://www.srl.caltech.edu/ACE/ASC/level2/index.html>) contains time averages of
152 the magnetic field over time periods 1 s, 16 s, 4 min, hourly, daily and 27 days (1 Bartels
153 rotation). In this work, IMF components (B_x , B_y , B_z) with time resolution of 16 s in
154 GSM coordinate systems are used.

155 We only work with 41 of 73 MCs identified by Huttunen et al. [2005] from March
156 1998 to December 2003: where the MCs were preceded by the plasma sheaths. We are
157 interested in comparing these two regions when it have been well identified. The 41 events

158 in chronological order are shown in Table 2 and 3. The columns from the left to the right
159 give: a numeration of the events, year, shock time (UT), MC start time (UT) and MC
160 end time (UT) respectively.

4. Methodology Using STE Analysis

161 Based on the description of MCs, a proper statistical tool can be used to identify their
162 typical features. The STE analysis was chosen to establish a methodology. The STE
163 analysis consists of a tool that compares the distribution of distances between all pairs
164 of vectors in the reconstructed state space with that of distances between different orbits
165 evolving in time. In this context, the terms “state space” and “orbits” are concepts of
166 the theory of chaotic dynamical systems. State space reconstruction is the first step in
167 non-linear time series analysis of data from chaotic systems including estimation of invari-
168 ants and prediction. Dynamical regimes, such as a resting state or periodic oscillation,
169 correspond to geometric objects, such as a point or a closed curve, in the phase space.
170 Evolution of a dynamical system corresponds to a trajectory (or an orbit) in the phase
171 space. Different initial states result in different trajectories. In the recurrence plot (RP) a
172 one-dimensional time series from a data file is expanded into a higher-dimensional space,
173 in which the dynamic of the underlying generator takes place. The concept of state space
174 and orbit are also valid in the RP and in the subsequent calculation of the STE. The STE
175 results identify in a certain objective way the characteristics of a physical process present
176 in a time measurement dataset.

177 The VRA software provides resources to investigate this promising approach immedi-
178 ately. The recurrence plot has been used. For more details, the information on it is
179 presented in Appendix A (recurrence plot) and Appendix B (entropy).

180 In this section, the purpose is to show the variation of STE values after processing
181 carried out in some synthetic time series, file included in VRA software. The methodology
182 to study synthetic time series will be implemented, with the purpose to be applied to
183 analyse IMF dataset.

4.1. STE Variations Versus Trend Angle

184 From an intuitive point of view, a time series is said to be stationary if there has not
185 trend and no systematic change in variance and if strictly periodic variations have been
186 removed [Chartfield, 2003]. Trend estimation is a statistical technique that could be aid in
187 the interpretation of data [Chartfield, 2003]. When a time series related to measurements
188 of a process are treated, trend estimation can be used to make and justify statements
189 about tendencies in the data. Given a set of data and the desire to produce some kind
190 of function fitted through of those data the simplest function to fit is a straight line
191 (using least-squares fit). If there is no global trend in time series the angle (“trend angle”)
192 between the straight line and the positive x axis must be zero.

193 We have calculated the STE value for each temporal series with embedding dimension
194 and time delay equal to 1 respectively. It may be noticed that STE value changes for dif-
195 ferent embedding parameters. For example, for Lorenz attractor (Lorenz data file included
196 in VRA), STE is near its minimum when the correct embedding is used (dimension = 3,
197 time delay = 16 to this particular data file). This and other results suggest that STE can
198 be used to determine the optimal embedding parameters, that is not the aim in this work.
199 We selected the same embedding and time delay, equal to one, to maintain equivalence
200 in the calculation of STE among all series in order to compare the results. Because our

201 hypothesis is that this tool (STE) could be useful in a computational implementation to
202 characterize MCs or used as a new property of them.

203 With the VRA software a group of synthetic time series were included. It were included
204 a variety of time series with different properties, i.e. periodic, random, with noises and
205 chaos respectively. A dataset of time series, Lorenz, Sine and White Noise, are used as
206 test cases to validate the STE calculation.

207 Figure 1 shows a time series plot of Lorenz data file included in VRA software. We gave
208 trends to the series through angular rotations about the origin. Time series have 3500
209 data records and it were rotated about the origin, angles of 0 rad , -0.01 rad , 0.01 rad
210 and 0.0175 rad respectively. The STE values have been calculated for each time series
211 and the results are shown in Table 4, row 2. In Table 4 in the five columns are shown:
212 time series data file included in VRA version 4.7; these time series are rotated about the
213 origin with [the previous angles](#); and it is calculated the STE values of each time series.

214 We follow the same idea, to cause a trend in time series for another cases, Sine and
215 White Noise data file also included in VRA software. The results have been included in
216 rows 3 and 4 in Table 4. In periodic time series (sine data file) the STE value is always zero
217 independently of increasing trend. In the other two cases, if time series trend increases
218 then the STE values decreases (see row 2 and 4 in Table 4). We are doing those kinds of
219 tests because we know that inside MCs the trend of IMF components increase; and we
220 are interested in knowing how it could affect STE values.

221 To go on with the above idea is good to know that: the time series of the first difference
222 is often enough to convert series with a trend into a stationary time series. The first-
223 order differences of time series values $x_1, x_2, x_3, \dots, x_N$ are given by a new series

224 y_1, y_2, \dots, y_{N-1} , where $y_{N-1} = x_N - x_{N-1}$. The operation $y_t = x_t - x_{t-1} = \nabla x_t$ is called
225 the first difference and ∇ is the difference operator [Chartfield, 2003].

226 Our interest is to study variations in the STE values when first-order differences are
227 applied on stationary time series. In time series studied previously (Lorenz, Sine and
228 White Noise), new time series from the first-order differences have been constructed.
229 After that, we calculated STE values of each time series and the results were compared
230 with the original series (non differentiated or untransformed) shown in Table 5. The
231 STE values are similar in both of them, *i.e.*, for transformed (first-order differences) and
232 untransformed time series. Thus, if the time series has non trend then the non-linear
233 delicate structures are not destroyed.

234 The STE value is low and may tend to zero in any time series with trend. [If there is a](#)
235 [trend in the time series, it could be removed by differencing the original time series before](#)
236 [calculating the STE. However, taking the first differences may interfere with the delicate](#)
237 [nonlinear structure in the time series \(if there is any\).](#) Thus STE values are calculated
238 on the untransformed series and then in the transformed series, where the first-order
239 differences is applied. This is done on a trial basis after calculating STE values of the
240 original series.

4.2. Variations Of STE Values Given By Time Series Size

241 The calculation of the STE with the VRA software, version 4.7, can not be made in
242 time series with size larger than ~ 5000 points because the STE has a rapid decrease
243 to zero. It seems to be a limitation of the software by some reason not explained in its
244 tutorial. To exemplify the previous statement, synthetic series have been created using
245 a [pseudorandom number generator \(PRNG\)](#) producing values in the range 0 to 1. In

246 Figure 2 (top panel), an example with 3000 points is shown. In this time series a STE
247 value of 86% was calculated. The Figure 2 (bottom panel) shows the plot of STE values
248 versus $\text{length}(X(t))$ of 18 time series constructed as shown in the top panel. The STE
249 values decrease in time series with a length larger than ~ 4000 points. When using the
250 VRA software someone must take into account this identified limitation in the extension
251 (length) of the data under analysis.

4.3. Scheme To Study STE Values In IMF Components

252 Figure 3 show the scheme that will be used to characterize MCs. From the 73 that have
253 been identified by Huttunen et al. [2005] from March 1998 to December 2003 are selected
254 41 of them, the cases where the plasma sheath also is identified. For both regions, time
255 series of IMF components with time resolution of 16 s, in GSM coordinates system, are
256 selected. Using VRA software the data without transformations are processed. Also the
257 same data before using the software are transformed. The aim of the transformations
258 is to eliminate the trend and noises respectively. The trends are eliminated with two
259 techniques, e.g. doing first order differences at time series and a rotation about the origin,
260 in the beginning of this section both techniques were explained. To filter the white noise
261 a Gaussian filter can be used, e.g. Mendes et al. [2006]. Inside the VRA software the RPs
262 are generated and the STE values are calculated.

263 Using a simple solution for a cylindrically symmetric force-free field with constant alpha
264 [Burlaga, 1988], time series were constructed. To a physical evaluation, the STE values
265 are calculated. Finally, with the results, the MCs are characterized.

5. Results And Discussion

266 The STE values for the 41 MC events are shown in Figure 4. At the top, the STE
 267 values calculated from the three IMF components B_x , B_y and B_z , plotted respectively as
 268 “o”, “+” and “x”, corresponding to MCs. At the bottom, the same of above but for
 269 the sheath regions. The STE values of the 246 time series ($3 * (41MCs + 41Shts) = 246$),
 270 were plotted in chronological order as appeared in Table 2 column 1. Some MCs do not
 271 have STE values close to zero in the three components simultaneously. Then, it is possible
 272 to find components with perfect structuredness (low STE) and absence of structure (high
 273 STE) in the same MC.

274 If STE values between the same components for the plasma sheath and the MC regions
 275 are compared (e.g. B_x -sheath ($STE = 56\%$) with B_x -cloud ($STE = 0\%$) in the event
 276 number 1), then in 5/41 (3/41) of the cases, in the B_x (B_y , B_z) component(s), the STE
 277 value in the MC is larger than at its plasma sheath region respectively. These are few
 278 cases, and show a clear tendency to decrease the STE value within the MC region in all
 279 IMF components. Someone can notice a clear tendency of the cloud events to present STE
 280 with lowest values, close to zero, as was noticed for B_z in Ojeda et al. [2005] and extended
 281 in this work, proposed as new feature adding to the usual features [Burlaga et al., 1981]
 282 established to the MCs.

283 Other interesting result is that STE values are zero in 20/41, 21/41, 26/41 MCs to
 284 B_x , B_y , B_z components respectively. The three components has zero entropy ($STE =$
 285 0%) at the same time in 17/41 MCs and 1/41 sheaths. The plasma sheath region with
 286 $STE = 0\%$ corresponds to event number 06 at Table 2.

287 Figure 5 shows a histogram of STE derived from Figure 4 for the B_z component corre-
 288 sponding to MCs (in black) and plasma sheaths (in grey) regions respectively. We have

37/41 or 90.2% of MCs with STE less than 40%. However, if we analyze the plasma sheath, then the result is exactly opposite, we found 37/41 or 90.2% of sheaths with STE larger than 40%. This shows the great difference between the two regions: the sheath is a turbulent region [Chian and Muñoz, 2011] where the plasma and magnetic field typically accumulate in ahead of the MC and cause fluctuations in the magnetic field. Thus, the time series could have more noise and therefore large STE values. In particular, the magnetic configuration of a MC could be described by a flux-rope with cylindrical geometry where the magnetic field has slow rotation along one day increasing the trend and decreasing the noise and therefore the STE values decrease. Low-entropy structures were found in the solar wind [e.g. Neugebauer et al., 2004], and physically we expected to find low entropy in the cloud. But the novel result shows that large amount of MCs with $STE = 0\%$ has been found.

We did some tests with time series to explain the above results. First, if the Gaussian noise is removed from the signal and the STE calculated, the STE value tend to decrease in less than 5% from its initial value. Second, when a trend is removed of the time series through a rotation (with the angle of slope line of best fit) the STE varies, but still the three components had $STE = 0\%$ at the same time in 17/41 MCs and 1/41 sheaths (see Figure 8, top panel). Third, by removing the trend through the first order difference in time series (see Figure 6). After that, there are still MCs with $STE = 0\%$.

In Figure 6 the study is the same as in Figure 4, but we have eliminated the trend through the first order difference in time series as mentioned in Section 4. In this case, most of calculating the STE values of all three components increased to $\sim 90\%$ in the plasma sheaths. Figure 7 shows a histogram of STE values in B_z component of MCs

312 and sheaths derived from Figure 6. If we eliminate the trend in the time series, then the
 313 STE value increase. Leaving now 11 of a total of 27 MCs (see Figure 5) with STE values
 314 between 0% and 10%. Also the STE increases in the MC region, but there are still MCs
 315 with zero STE value.

316 Due to a software limitation, presented earlier (Figure 2), we investigated the effect of
 317 the length of the time series that have studied in Figure 4. Then, in Figure 8 (top panel),
 318 a plot of STE versus length of B_z time series for all MCs are shown. The “o” and “+”
 319 symbols correspond to the original and transformed (removing the Gaussian noise and
 320 “trend” through a rotation about the origin) time series respectively. A vertical line was
 321 drawn in the point with $length(B_z) = 5500$ points. To the right of the vertical line, due
 322 to a software limitation (this was discussed in the end of section 4) the STE value is zero.

323 In Figure 8 (bottom panel) the histogram of the original or untransformed time series
 324 helps to identify overlapping points of MC that are shown in the top panel. Exist a total
 325 number of 17/41 MCs with zero STE values to the right of the vertical line. These are
 326 the events 1 – 4, 6 – 10, 13, 16, 27, 30, 33 – 35, 40 shown in Table 2. This is a problem
 327 because the larger MCs are just the best structured. However, there still 9/41 MCs with
 328 zero STE values to the left of the vertical line, these are the events 5, 12, 21, 23 – 25,
 329 31, 32, 37 shown in Table 2. Event No. 38 has $STE = 6\%$ and complete the total of 27
 330 events with STE between 0 – 10% shown in the histogram at Figure 5.

331 In Figure 8 the STE values of the transformed time series (“+” symbol) increase and
 332 are different from zero in the MC with less than 5500 points. The smooth increase of
 333 trend occur in time series of IMF in a MC and is caused by the travel of an organized
 334 structure in form of flux-rope, crossing the spacecraft. The trend grows smoothly for the

335 IMF in a MC with length less than 5500 and are the main causes of lower STE values.
336 Since the STE results of this tool can be affected by the trend, this tool could be useful in
337 computational applications to identify MC regions, but failed to identify the boundaries
338 of them.

339 In Figure 9 the study is the same as in Figure 8, but for the plasma sheaths regions.
340 The length of the sheaths have less points than the MCs, only one sheath had more than
341 5500 points, the event number 6 shown in Table 2. Both histograms at the Figures 8 and
342 9 are constructed only to help in the visualization of the distribution of lengths at the top
343 panels of it. The main result is that the STE values in the sheaths, of the transformed
344 time series (“+” symbol), are approximately the same as the original (“o” symbol) time
345 series. We conclude that the trend in the plasma sheath is less important and STE have
346 large values.

347 To study the true STE values of the MC with more than 5500 points and overcome the
348 software limitation, we have two options: (1) select data with other temporal resolution
349 (i.e., it to become poor the data information); or (2) select a MC sample with less than
350 5500 points. We performed option 2, taking the intervals from the positions 500 (to avoid
351 effects caused by the identification of the boundaries) to 4500 in IMF B_z . Thus, the length
352 of the time series reconstructed is 4001 data points. These 17/41 cases represented by
353 “×” symbol are shown in Figure 10 (top panel); the “o” symbol represent non-transform
354 MCs similar to 8. In the right hand of the vertical line, the MCs sample (“×” symbol
355 and 4001 data points) are plotted in the position with same length of non-transform MCs
356 (“o”). Only 1/17 case remains with zero STE and a total of 4/17 events remains with
357 STE less than 11%. To make a better comparison, the histogram in the bottom panel at

358 Figure 10 was built. We have 33/41 or 80.5% of MCs with STE less than 40%. Still a
359 good percentage (80.5%) that enables us to keep the findings of low STE in MCs.

360 A physical interpretation can be established as following. It was observed during the
361 data processing that entropy values less than 40% could appear only in one or two of the
362 three components of the MCs. This has a physical explanation: magnetic field axis of
363 a magnetic flux-rope in a MC could have different inclinations. Then, the trend of IMF
364 components is larger in a plane or one direction. It is advisable to work in a reference
365 frame found by a MVA analysis. So far, we have been seeking the causes of the large
366 amount of MCs with $STE = 0\%$. During a MC, the magnetic field strength is higher
367 than the average, the magnetic field direction rotates smoothly through a large angle,
368 then the periods with MCs present more trend in the magnetic behavior than the periods
369 of sheaths or quiet SW. The trend is the principal cause of the lower STE values in MC.

370 To demonstrate quantitatively all results that have been shown up here, a simple
371 solution for a cylindrically symmetric force-free field with constant alpha [Lundquist,
372 1950, 1951] was studied. Burlaga [1988] studied the above solution with constant alpha
373 to describe the types of signatures observed in the SW at 1 AU when MCs travel through
374 of a spacecraft. He concluded that the observed magnetic field profiles depend on the
375 position and orientation of the axis of the MC. We written the force-free model solution

376 as Burlaga [1988]:

$$\text{Axial component : } B_A = B_0 J_0(\alpha R),$$

$$\text{Tangential component : } B_T = B_0 H J_1(\alpha R),$$

$$\text{Radial component : } B_R = 0,$$

$$\text{Total magnetic field : } B = \sqrt{B_A^2 + B_T^2 + B_R^2}, \quad (1)$$

377 where $H = \pm 1$, the sign providing the handedness of the field helicity, and where B_0
 378 is an estimate of field at the axis of the cloud and R is the radial distance from the
 379 axis, J_0 and J_1 are the Bessel function of the first kind of order 0 and 1. The above
 380 equations were plotted in Figure 11. The magnitude of the magnetic field at any instant
 381 is B , which decreases from a maximum B_{max} on the axis of the MC to $\sim 0.5B_{max}$ at the
 382 outer boundary. Following Burlaga [1988], we show the boundaries with two vertical line
 383 in Figure 11 as the points where $B_A = 0$, i.e. where $\alpha \cdot R = 2.4$ and $B/B_0 = 0.5$.

384 Time series with 2001 points inside the boundaries of the cloud shown in Figure 11
 385 are constructed. On other hand, we obtained the recurrence plots of B_A , B_T and B
 386 respectively. After that, the STE values are calculated; with the STE of $B_A = 27\%$; STE
 387 of $B_T = 0\%$; STE of $B = 25\%$.

388 Those low STE values are the physical justification of our results. If the spacecraft
 389 crosses near the cloud axis then zero entropy values of some IMF components of the
 390 structure are consequences of a nearly cylindrically symmetric force-free field. These
 391 results reinforce our initial hypothesis that STE could be established as a feature or
 392 tool to help in analysis of IMF data for the MC identification, mainly when the only
 393 measurements obtained by satellites are the IMF.

6. Conclusions

394 In this work, using the recurrence plot (RP) technique, a methodological approach is
395 established in order to obtain the spatio-temporal entropy (STE) related to magnetic
396 cloud (MC) periods. The method presented in Eugene Kononov's VRA software provides
397 resource for this kind of analysis. For this investigation, the interplanetary magnetic fields
398 from a complete solar wind data framework are investigated.

399 The analyses developed show that the STE values for MCs are lower than the ones for
400 sheath region or the solar wind background.

401 The reason is that in MC the magnetic field strength is higher than the average, the
402 magnetic field direction rotates smoothly through a large angle. Then periods of MCs have
403 more trend than sheaths region and quiet SW periods. The trend is the principal cause of
404 the lower values of STE. It can be noticed that inside MC the IMF have less fluctuations
405 and less noise than outside its boundary. **MCs have magnetic field more structured than**
406 **sheath and quiet SW**. This also collaborates for the decrease of STE within the MC region.

407 Also, the differences among the STE values for the three magnetic components in a MC
408 give an idea about the anisotropy in the structure of MCs. Those features are related to the
409 flux-rope structure orientation, based on concepts as presented by Bothmer and Schwenn
410 [1994, 1998]. By using a force free model for IMF as presented by Burlaga [1988], a test
411 considering the magnetic components, mainly the tangential component, of a cylindrically
412 symmetric force-free field constructed analytically results zero STE value. It agrees with
413 the physical assumption of finding zero STE values when studying experimental data in
414 MC periods.

415 The new feature just examined here adds to the usual features, as described in Burlaga
416 et al. [1981], for the characterization of MCs. Thus, the STE calculation can be an
417 auxiliary objective tool to identify flux-ropes associated with MCs, mainly during events
418 with no available plasma data but only with IMF.

Appendix A: The Recurrence Plots In Visual Recurrence Analysis Software

419 A summary of the ideas expressed in the Eugene Kononov's Visual Recurrence Analysis
420 (VRA) software (VRA v4.7 <http://nonlinear.110mb.com/vra/>) about recurrence plots
421 (RPs) is presented. In order to present the ideas, some figures are used to guide the
422 description. Figure 12 (top panel) shows a recurrence plot (RP) for a simple sine wave,
423 using the data file just included in VRA software. In it organized patterns of color
424 characteristics are shown for the periodical signal. In order to allow a comparative view,
425 a RP of white noise is shown in Figure 12 (bottom panel), with the data file also included.
426 With a different result, an uniform distribution of color characteristics is noticed for the
427 random signal.

428 The RP is a relatively recent technique for the qualitative assessment of time series [Eck-
429 mann et al., 1987]. This technique allows someone detects hidden patterns and structural
430 changes in data or see similarities in patterns across the time series under analysis using
431 graphical representation. The fundamental assumption underlying the idea is that an
432 observable time series (a sequence of observations) is the manifestation of some dynamic
433 process.

434 It has been proved mathematically that one can recreate a topologically equivalent
435 picture of the original multidimensional system behavior by using the time series of a
436 single observable variable [Takens, 1981]. The basic idea is that the effect of all the

437 other (unobserved) variables is already reflected in the series of the observed output.
 438 Furthermore, the rules that govern the behavior of the original system can be recovered
 439 from its output.

440 In the RPs a one-dimensional time series from a data file is expanded into a higher-
 441 dimensional space, in which the dynamic of the underlying generator takes place. This
 442 is done by a technique called “delayed coordinate embedding”, which recreates a phase
 443 space portrait of the dynamical system under study from a single (scalar) time series.
 444 To expand a one-dimensional signal into an M-dimensional phase space, one substitutes
 445 each observation in the original signal $X(t)$ with vector $(y(i) = \{x(i), x(i - d), x(i - 2d),$
 446 $\dots, x(i - (m - 1)d\})$, where i is the time index, m is the embedding dimension, d is the time
 447 delay. As a result, we have a series of vectors $Y = y(1), y(2), y(3), \dots, y(N - (m - 1)d)$,
 448 where N is the length of the original series.

449 With such reconstruction it is possible to reproduce the original system states at
 450 each time where we have an observation of that system output. Each unknown
 451 state $Z(t)$ at time t is approximated by a vector of delayed coordinates $Y(t) =$
 452 $x(t), x(t - d), x(t - 2d), \dots, x(t - (m - 1)d$. After the Euclidean distances between all
 453 vectors are calculated, they are mapped to colors from the pre-defined color map and are
 454 displayed as colored pixels in their corresponding places (see Figure 12 (top panel), for
 455 example). The RP is a graphical representation of a correlation integral. The important
 456 distinction (and an advantage) is that the RP, unlike the correlation integrals, preserve
 457 the temporal dependence in the time series, in addition to the spatial dependence.

458 In RPs, if the underlying signal is truly random and has no structure, the distribution
 459 of colors is uniform and does not have any identifiable patterns (see Figure 12 (bottom

460 panel), for example). There is some determinism in the signal generator, which can be
461 detected by some distinctive color distribution. For example, hot colors (yellow, red, and
462 orange) can be associated with small distances between the vectors, while others colors
463 (blue, black) may be used to show large distances. In this printed work colors are noticed
464 as a grey pattern (from white to black). Therefore one can visualize and study the motion
465 of the system trajectories and infer some characteristics of the dynamical system that
466 generated the time series. Also, the length of diagonal line segments of the same color
467 on the RP brings an idea about the signal predictability. But, RP is mostly a qualitative
468 tool.

469 For random signals, the uniform (even) distribution of colors over the entire RP is
470 expected. The more deterministic the signal, the more structured the RP. So for the
471 purpose of comparison in Figure 12 (top panel) the RP of a strictly periodic signal can
472 see and in Figure 12 (bottom panel) the RP of the white noise time series.

473 For force-free model solution, the recurrence plots of B_A , B_T are shown at Figures 13,
474 top and bottom panels respectively.

Appendix B: The Entropy Concepts In Recurrence Plot

475 The RP is a visual tool for the investigation of temporal recurrence in phase space
476 [Takens, 1981]. With the purpose of reaching a quantitative tool in this work, a brief
477 review about some methods to calculate the entropy in the RP and the phase space is
478 presented here.

479 The calculation of the spatio-temporal entropy, called in short way as STE was used
480 to measures the image “structuredness” in a bidimensional representation, *i.e.*, both in
481 “space” and time domains. Its implementation in VRA software is to quantify the order

482 found in RPs. The result is normalized and presented as a percentage of “maximum”
 483 entropy (randomness). When the entropy has a value of 100% it means the absence of any
 484 structure whatsoever (uniform distribution of colors, pure randomness, seen in Figure 12
 485 (bottom panel)). **In particular**, 0% of entropy implies “perfect” structure (distinct color
 486 patterns, perfect “structuredness” and predictability, seen in Figure 12 (top panel)).

487 Recurrence is the most important feature of chaotic systems [Eckmann et al., 1987].
 488 The popularity of RPs lies in the fact that their structures are visually appealing, and
 489 that they allow the investigation of high dimensional dynamics by means of a simple two-
 490 dimensional plot [Facchini et al., 2009]. For a better understanding and quantification
 491 of the recurrences, Webber and Zbilut [1994] have proposed a set of quantification mea-
 492 sures, which are mainly based on the statistical distribution of the line structures in the
 493 RP. Recurrence quantification analysis (RQA) is a nonlinear technique used to quantify
 494 the information supplied by a RP [Zbilut and Webber, 1992; Webber and Zbilut, 1994].
 495 Recurrence variables are calculated from the upper triangular area of the recurrence plot,
 496 excluding the central diagonal, because the plot is symmetrical about the main diagonal.
 497 The RQA can be used as a tool for the exploration of bifurcation phenomena and dynam-
 498 ics changes also in nonstationary and short time series. The entropy (ENT) is one of the
 499 recurrence variables of the RQA method. It is the Shannon information entropy for the
 500 distribution probability of the diagonal lines. That is:

$$ENT = - \sum_{k=L_{min}, p(k) \neq 0}^{L_{max}} p(k) \log_2(p(k)), \quad (B1)$$

501 where L_{min} is the minimum length of diagonal lines in RP and

$$p(k) = \frac{\text{number of diagonal lines of length } k \text{ in RP}}{\text{number of diagonal lines in RP}}. \quad (B2)$$

502 The ENT can be calculated using the VRA software; but it should not be confused with
503 the STE.

504 Little et al. [2007] developed a Recurrence Period Density Entropy (RPDE) method,
505 first it requires the embedding of a time series in phase space, which, according to Taken's
506 embedding theorems, can be carried out by forming time-delayed vectors for each value
507 x_n in the time series. Then, around each point in the embedded phase space, a recurrence
508 neighbourhood of radius ϵ is created. All recurrences into this neighbourhood are tracked,
509 and the time interval T between recurrences is recorded in a histogram. This histogram
510 is normalized to create an estimate of the recurrence period density function $p(T)$. The
511 normalized entropy of this density is the RPDE value H_{norm} [Little et al., 2007].

$$H_{norm} = -(\ln(T_{max}))^{-1} \sum_{t=1}^{T_{max}} p(t) \ln(p(t)). \quad (\text{B3})$$

512 The RPDE value is a scalar in the range zero to one. For purely periodic signals,
513 $H_{norm} = 0$ (STE=0%) whereas for purely uniform white noise, $H_{norm} = 1$ (STE=100%).
514 However, estimates obtained with this technique (RPDE) are different from those obtained
515 with the STE.

516 Dasan et al. [2002] report an analysis, using the tools of nonlinear dynamics and chaos
517 theory, of the fluctuations in the stress determined from simulations of shear flow of
518 Stokesian suspensions. They also computed the STE using VRA for the stress. The
519 calculated values of the STE for the shear and normal stresses were nearly zero, showing
520 perfect structure in the data. They observed definite structure in the phase-space plot of
521 the stress components [Dasan et al., 2002]. They cited the works of Peacock [1983]; Carr
522 and Schwartz [1998]. Peacock [1983] presented a two-dimensional analogue of Kolmogorov-

523 Smirnov test, useful for analysing the distribution of data in two dimensions, as is the
 524 RP. Carr and Schwartz [1998] investigated the fluctuation phenomena in plasmas that
 525 often needs the analysis of spatio-temporal signals. It was shown how such signals can be
 526 analyzed using the biorthogonal decomposition, which splits them into orthogonal spatial
 527 and temporal modes. Several parameters allow one to quantify the weight distribution in
 528 the biorthogonal decomposition. The total energy of spatio-temporal signal is found to
 529 be equal to the sum of the eigenvalues, α_m :

$$E(u) = \sum_{m=1}^N \alpha_m^2. \quad (\text{B4})$$

530 They can define the relative energy of the m^{th} structure as

$$E_m(u) = \frac{\alpha_m^2}{E(u)}, \quad (\text{B5})$$

531 and the entropy of the spatio-temporal signal $u(t, j)$ is defined as

$$H(u) = -\frac{1}{\log N} \sum_{m=1}^N E_m(u) \log E_m(u). \quad (\text{B6})$$

532 It describes how the energy is distributed across the N_s significant structures. Signal whose
 533 energy is concentrated in a single structure such that $N_s = 1$ will have very low entropy
 534 $H(u) = 0$, or $H(u) = 1$ if the energy is distributed equally among the N_s significant
 535 structures. Further, the results presented in this paper shows the usefulness of STE
 536 implemented by Eugene Kononov's software to study MCs.

537 **Acknowledgments.** This work was supported by grants from CNPq (grants
 538 483226/2011-4, 307511/2010-3, 306828/2010-3 and 486165/2006-0), FAPESP (grants
 539 2012/072812-2 and 2007/07723-7) and CAPES (grants 1236-83/2012 and 86/2010-29).
 540 Arian Ojeda González thanks the CAPES and CNPq (grant 141549/2010-6) for his PhD

541 scholarship and CNPq (grant 150595/2013-1) for his postdoctoral research support. We
542 are grateful to V. E. Menconi (FAPESP grant 2008/09736-1) for their helpful computa-
543 tional assistance. We also wish to thank the anonymous referees for improvement of this
544 paper. Acknowledgments to Eugene Kononov, author of the Visual Recurrence Analy-
545 sis software. Also, the authors would like to thank ACE science team members for the
546 datasets used in this work.

References

- 547 Bothmer, V., Rust, D. M., 1997. The field configuration of magnetic clouds and the solar
548 cycle. *Geophysical Monograph* 99, 139–146, AGU.
- 549 Bothmer, V., Schwenn, R., 1994. Eruptive prominences as sources of magnetic clouds in
550 the solar wind. *Space Science Reviews* 70, 215.
- 551 Bothmer, V., Schwenn, R., 1998. The structure and origin of magnetic clouds in the solar
552 wind. *Annales Geophysicae* 16, 1–24, 10.1007/s00585-997-0001-x.
- 553 Burlaga, L., Behannon, K., 1982. Magnetic clouds: Voyager observations between 2 and
554 4 AU. *Solar Physics* 81, 181.
- 555 Burlaga, L. F., 1988. Magnetic clouds and force-free fields with constant alpha. *Journal*
556 *of Geophysical Research* 93 (7), 7217–7224.
- 557 Burlaga, L. F., Klein, L. W., Mar. 1980. Magnetic clouds in the solar wind. NASA Tech.
558 Memo (80668), 1–15.
- 559 Burlaga, L. F., Sittler, E., Mariani, F., Schwenn, R., 1981. Magnetic loop behind an
560 interplanetary shock: Voyager, Helios and IMP 8 observations. *Journal of Geophysical*
561 *Research* 86, 6673–6684.

- 562 Carr, T. W., Schwartz, I. B., 1998. On measures of disorder in globally coupled oscillators.
563 *Physica D* 115, 321–340.
- 564 Chartfield, C., Jul. 2003. *The analysis of time series an introduction*, sixth Edition. Chap-
565 man & Hall/CRC Texts in Statistical Science). Taylor & Francis e-Library, 2009.
- 566 Chian, A. C.-L., Muñoz, P. R., 2011. Detection of Current Sheets and Magnetic Recon-
567 nections at the Turbulent Leading Edge of an Interplanetary Coronal Mass Ejection.
568 *The Astrophysical Journal Letters* 733 (2), L34.
- 569 Cocconi, G., Greisen, K., Morrison, P., Gold, T., Hayakawa, S., 1958. The cosmic ray
570 flare effect. *Il Nuovo Cimento*(1955-1965) 8, 161–168.
- 571 Dasan, J., Ramamohan, T. R., Singh, A., Nott, P. R., 2002. Stress fluctuations in sheared
572 Stokesian suspensions. *Physical Review E* 66 (2), 021409.
- 573 Démoulin, P., Dasso, S., May 2009. Causes and consequences of magnetic cloud expansion.
574 *Astronomy and Astrophysics* 498 (2), 551–566.
- 575 Eckmann, J., Kamphorst, S., Ruelle, D., 1987. Recurrence plots of dynamical systems.
576 *Europhysics Letters* 4 (9), 973–977.
- 577 Facchini, A., Mocenni, C., Vinicio, A., 2009. Generalized recurrence plots for the analysis
578 of images from spatially distributed systems. *Physica D* 238, 162–169.
- 579 Goldstein, H., 1983. On the field configuration in magnetic clouds. *Solar Wind Five*, 731.
- 580 Gosling, J., 1990. Coronal mass ejections and magnetic flux ropes in interplanetary space.
581 In: Russel, C. T., Priest, E. R., Lee, L. C. (Eds.), *Physics of Magnetic Flux Ropes*.
582 AGU Geophys. Monogr., p. 343.
- 583 Hidalgo, M. A., 2003. A study of the expansion and distortion of the cross section of mag-
584 netic clouds in the interplanetary medium. *Journal of Geophysical Research* 108 (A8).

- 585 Hidalgo, M. A., Mar. 2005. Correction to “A study of the expansion and distortion of the
586 cross section of magnetic clouds in the interplanetary medium”. *Journal of Geophysical*
587 *Research (Space Physics)* 110, 3207.
- 588 Huttunen, K. E. J., Bothmer, V., Koskinen, H. E. J., 2005. Properties and geoeffectiveness
589 of magnetic clouds in the rising, maximum and early declining phases of solar cycle 23.
590 *Annales Geophysicae* 23, 1–17.
- 591 Ivanov, K., Harshiladze, A., 1984. Dynamics of hydromagnetic clouds from powerful solar
592 flares. *Solar Physics* 92, 351.
- 593 Klein, L. W., Burlaga, L. F., 1982. Interplanetary magnetic clouds at 1 AU. *Journal of*
594 *Geophysical Research* 87, 613–624.
- 595 Lepping, R. P., Behannon, K. W., Jun. 1979. Magnetic field directional discontinuities. 1:
596 Minimum variance errors. NASA STI/Recon Technical Report N 79, 31116.
- 597 Lepping, R. P., Burlaga, L. F., Jones, J. A., Aug. 1990. Magnetic field structure of inter-
598 planetary magnetic clouds at 1 AU. *Journal of Geophysical Research* 951, 11957–11965.
- 599 Little, M. A., McSharry, P. E., J., R. S., Costello, D. A., Moroz, I. M., 2007. Exploit-
600 ing Nonlinear Recurrence and Fractal Scaling Properties for Voice Disorder Detection.
601 *BioMedical Engineering OnLine*.
- 602 Lundquist, S., 1950. Magneto-hydrostatic fields. *Ark Fys* 2, 361–365.
- 603 Lundquist, S., Jul. 1951. On the Stability of Magneto-Hydrostatic Fields. *Physical Review*
604 83, 307–311.
- 605 Lynch, B., Zurbuchen, T., Fisk, L., Antiochos, S., 2003. Internal structure of magnetic
606 clouds: Plasma and composition. *Journal of Geophysical Research* 108 (A6), 1239–1253.

- 607 Ma, Y., Zhang, H., 2001. Detecting motion object by Spatial-Temporal Entropy. In: IEEE
608 International Conference on Multimedia and Expo, 2001. pp. 265–268.
- 609 Marubashi, K., 1986. Structure of the interplanetary magnetic clouds and their solar
610 origins. *Advances in Space Research* 6 (6), 335–338.
- 611 McComas, D. J., Bame, S. J., Barker, P., Feldman, W. C., Phillips, J. L., Riley, P.,
612 Griffee, J. W., Jul. 1998. Solar Wind Electron Proton Alpha Monitor (SWEPAM) for
613 the Advanced Composition Explorer. *Space Science Reviews* 86, 563–612.
- 614 Mendes, O., Mendes da Costa, A., Bertoni F., 2006. Effects of the number of stations and
615 time resolution on Dst derivation. *Journal of Atmospheric and Solar-Terrestrial Physics*
616 68(18):2127-2137, doi: 10.1016/j.jastp.2006.01.015.
- 617 Morrison, P., 1954. Solar-connected variations of the cosmic rays. *Physical Reviews* 95,
618 646.
- 619 Mulligan, T., Russel, C. T., Luhmann, J., 1998. Solar cycle evolution of the structure of
620 magnetic clouds in the inner Heliosphere. *Geophysical Research Letters* 25 (15), 2959–
621 2962.
- 622 Neugebauer, M., Liewer, P. C., Goldstein, B., Zhou, X., Steinberg, J. T., Oct. 2004.
623 Solar wind stream interaction regions without sector boundaries. *Journal of Geophysical*
624 *Research* 109 (A10102), 102.
- 625 Nieves-Chinchilla, T., Hidalgo, M., Sequeiros, J., 2005. Magnetic Clouds Observed at 1
626 Au During the Period 2000–2003. *Solar Physics* 232, 105–126.
- 627 Ojeda, G. A., Calzadilla, A., Lazo, B., Alazo, K., Savio, S., 2005. Analysis of Behavior of
628 Solar Wind Parameters Under Different IMF Conditions Using Two Nonlinear Dynamics
629 Techniques. *Journal of Atmospheric and Solar-Terrestrial Physics* 67, 1859–1864.

- 630 Peacock, J. A., Feb. 1983. Two-dimensional goodness-of-fit testing in astronomy. Royal
631 Astronomical Society 202 (1983), 615–627.
- 632 Piddington, J. H., 1958. Interplanetary Magnetic Field and Its Control of Cosmic-Ray
633 Variations. *Physical Reviews* 112, 589.
- 634 Sonnerup, B., Cahill, L., 1967. Magnetopause structure and attitude from Explorer 12
635 observations. *Journal of Geophysical Research* 72, 171.
- 636 Schwenn, R., 2006. Space weather: The Solar Perspective. *Living reviews in solar physics*
637 3 (2), 1–72.
- 638 Smith, C. W., L’Heureux, J., Ness, N. F., Acuña, M. H., Burlaga, L. F., Scheifele, J.,
639 1998. The ACE Magnetic Fields Experiment. *Space Science Reviews*, v. 86, p. 613–632.
- 640 Takens, F., 1981. Detecting strange attractors in turbulence. *Lecture Notes in Mathemat-*
641 *ics*, 366–381.
- 642 Webber, C. L., Zbilut, L. P., 1994. Dynamical assessment of physiological systems and
643 state using recurrence plot strategies. *Journal of Applied Physiology* 76, 965–973.
- 644 Wu, C.-C., Lepping, R. P., Gopalswamy, N., Sep. 2003. Variations of magnetic clouds and
645 CMEs with solar activity cycle. In: Wilson, A. (Ed.), *Solar Variability as an Input to*
646 *the Earth’s Environment*. Vol. 535 of ESA Special Publication. pp. 429–432.
- 647 Zbilut, L. P., Webber, C. L., 1992. Embeddings and delays as derived from quantification
648 of recurrence plots. *Physics Letters A* 171, 199–203. 2101

Table 1. Summary of seven previous studies that identified MCs before 2003. In column one: 1- Bothmer and Rust [1997], 2- Bothmer and Schwenn [1998], 3- Mulligan et al. [1998], 4- Lynch et al. [2003], 5- Wu et al. [2003], 6- Huttunen et al. [2005], 7- Nieves-Chinchilla et al. [2005].

Paper	Period	T_t (years)	Spac ^f	MC
1	1965-1993	28	OMNI	67
2	12/1974-07/1981	6.7	Helios 1/2	45
3	1979-1988	10	Pioneer	61
4	02/1998-07/2001	3.5	ACE	56
5	1995-2002	8	WIND	71
6	1997-2003	7	WIND/ACE	73
7	2000-2003	4	WIND/ACE	35

^a SOURCE: Adapted from Huttunen et al. [2005].

Table 2. Solar Wind data studied (from Huttunen et al. [2005]).

No.	Year	Shock	UT	Start	UT	Stop	UT
01	1998	06 Jan	13:19	07 Jan	03:00	08 Jan	09:00
02		03 Feb	13:09	04 Feb	05:00	05 Feb	14:00
03		04 Mar	11:03	04 Mar	15:00	05 Mar	21:00
04		01 May	21:11	02 May	12:00	03 May	17:00
05		13 Jun	18:25	14 Jun	02:00	14 Jun	24:00
06		19 Aug	05:30	20 Aug	08:00	21 Aug	18:00
07		24 Sep	23:15	25 Sep	08:00	26 Sep	12:00
08		18 Oct	19:00	19 Oct	04:00	20 Oct	06:00
09		08 Nov	04:20	08 Nov	23:00	10 Nov	01:00
10		13 Nov	00:53	13 Nov	04:00	14 Nov	06:00
11	1999	18 Feb	02:08	18 Feb	14:00	19 Feb	11:00
12		16 Apr	10:47	16 Apr	20:00	17 Apr	18:00
13		08 Aug	17:45	09 Aug	10:00	10 Aug	14:00
14	2000	11 Feb	23:23	12 Feb	12:00	12 Feb	24:00
15		20 Feb	20:57	21 Feb	14:00	22 Feb	12:00
16		11 Jul	11:22	11 Jul	23:00	13 Jul	02:00
17		13 Jul	09:11	13 Jul	15:00	13 Jul	24:00
18		15 Jul	14:18	15 Jul	19:00	16 Jul	12:00
19		28 Jul	05:53	28 Jul	18:00	29 Jul	10:00
20		10 Aug	04:07	10 Aug	20:00	11 Aug	08:00
21		11 Aug	18:19	12 Aug	05:00	13 Aug	02:00

Continue

Table 3. Continuation of Table 2.

No.	Year	Shock	UT	Start	UT	Stop	UT
22		17 Sep	17:00	17 Sep	23:00	18 Sep	14:00
23		02 Oct	23:58	03 Oct	15:00	04 Oct	14:00
24		12 Oct	21:36	13 Oct	17:00	14 Oct	13:00
25		28 Oct	09:01	28 Oct	24:00	29 Oct	23:00
26		06 Nov	09:08	06 Nov	22:00	07 Nov	15:00
27	2001	19 Mar	10:12	19 Mar	22:00	21 Mar	23:00
28		27 Mar	17:02	27 Mar	22:00	28 Mar	05:00
29		11 Apr	15:18	12 Apr	10:00	13 Apr	06:00
30		21 Apr	15:06	21 Apr	23:00	22 Apr	24:00
31		28 Apr	04:31	28 Apr	24:00	29 Apr	13:00
32		27 May	14:17	28 May	11:00	29 May	06:00
33		31 Oct	12:53	31 Oct	22:00	02 Nov	04:00
34	2002	23 Mar	10:53	24 Mar	10:00	25 Mar	12:00
35		17 Apr	10:20	17 Apr	24:00	19 Apr	01:00
36		18 May	19:44	19 May	04:00	19 May	22:00
37		01 Aug	23:10	02 Aug	06:00	02 Aug	22:00
38		30 Sep	07:55	30 Sep	23:00	01 Oct	15:00
39	2003	20 Mar	04:20	20 Mar	13:00	20 Mar	22:00
40		17 Aug	13:41	18 Aug	06:00	19 Aug	11:00
41		20 Nov	07:27	20 Nov	11:00	21 Nov	01:00

END

Table 4. STE values related to trends for three time series with data file included in VRA

4.7.

Series/angle (rad)	0	-0.01	0.01	0.0175
STE(Lorenz):	73%	30%	29%	0%
STE(Sine):	0%	0%	0%	0%
STE(White Noise):	80%	34%	34%	3%

Table 5. STE values related to the first-order differences in time series.

Series	Untransformed	first-order differences
STE(Lorenz)	73%	75%
STE(Sine)	0%	0%
STE(White Noise)	80%	82%

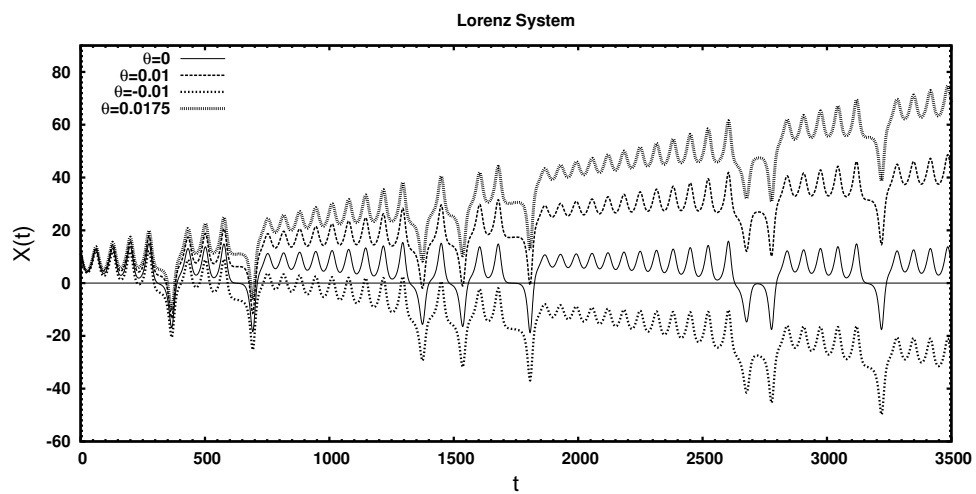


Figure 1. Time series plot of Lorenz data file included in VRA (case with $\theta = 0$). Series rotated about origin ($\theta = -0.01$ rad , $\theta = 0.01$ rad , $\theta = 0.0175$ rad) and the three resulting series also plotted. After that, we calculate the STE of each time series.

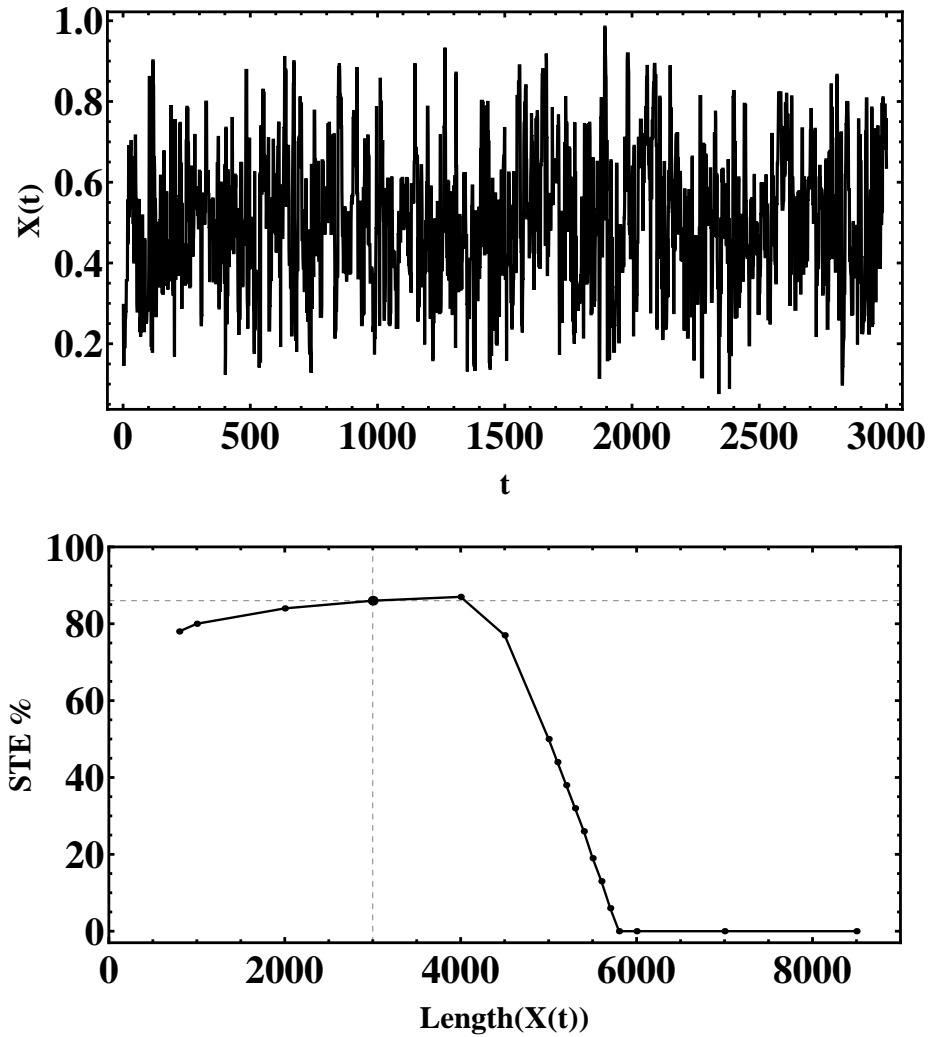


Figure 2. (top panel) $X(t)$ vs t is plotted, where $X(t)$ is a synthetic series created using a pseudorandom number generator producing values in the range 0 to 1. A simple moving average is applied to show the graph. The time series of pseudorandom number has a recurrence plot similar to shown at Figure 12 (bottom panel) and STE value of this time series is 86%. (bottom panel) The STE values versus $\text{length}(X(t))$ of time series constructed. These values decrease in time series with a length larger than ~ 4000 points.

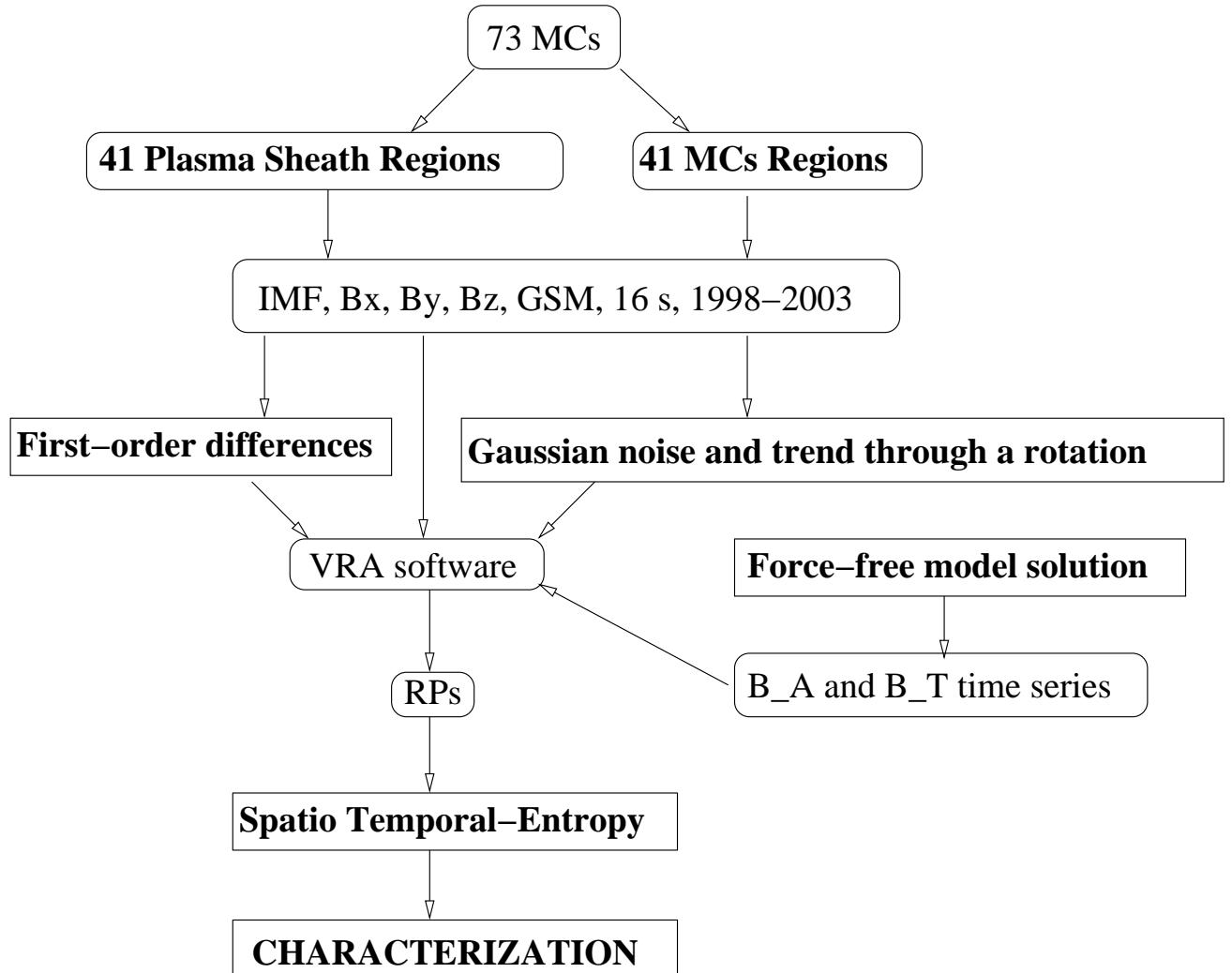


Figure 3. Scheme used to study 41 MCs in Section 5.

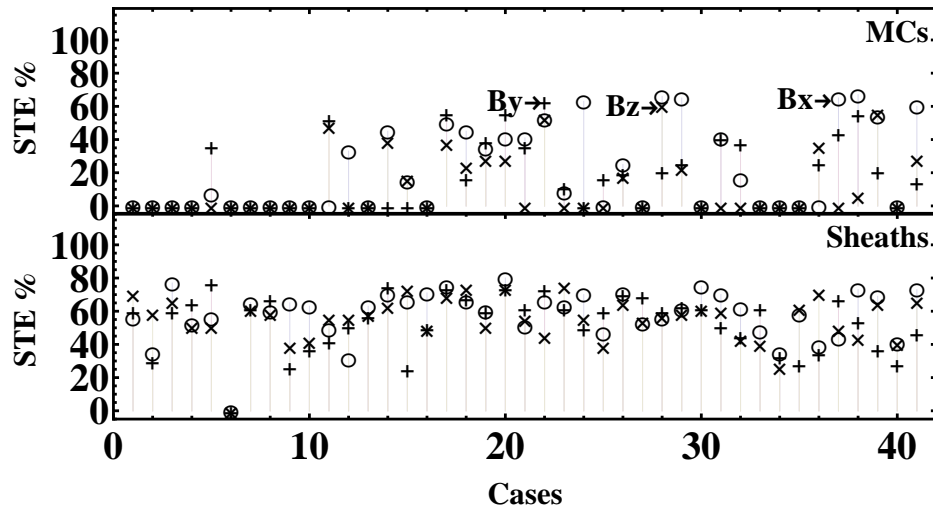


Figure 4. The STE values for 41 MCs from 1998 to 2003 that were presented in Table 2. At the top, the STE values for the three IMF components (“o” $\equiv B_x$, “+” $\equiv B_y$, “x” $\equiv B_z$) versus cases as shown in Table 2. At bottom, the same as to above but for the sheath regions. In the two panels without previous transformation in the time series.

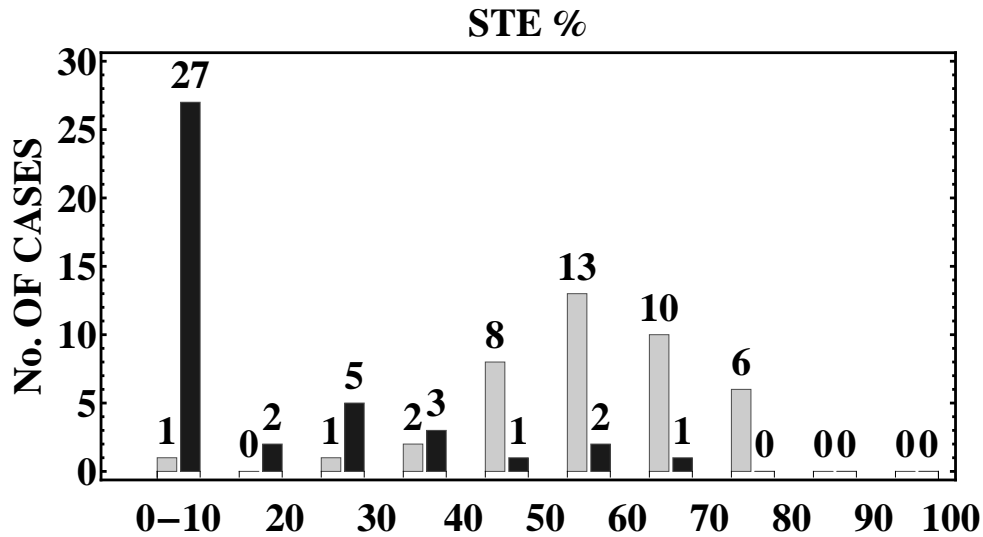


Figure 5. A histogram of STE derived from Figure 4 for B_z corresponding to MCs regions (in black) and plasma sheaths regions (in grey) respectively.

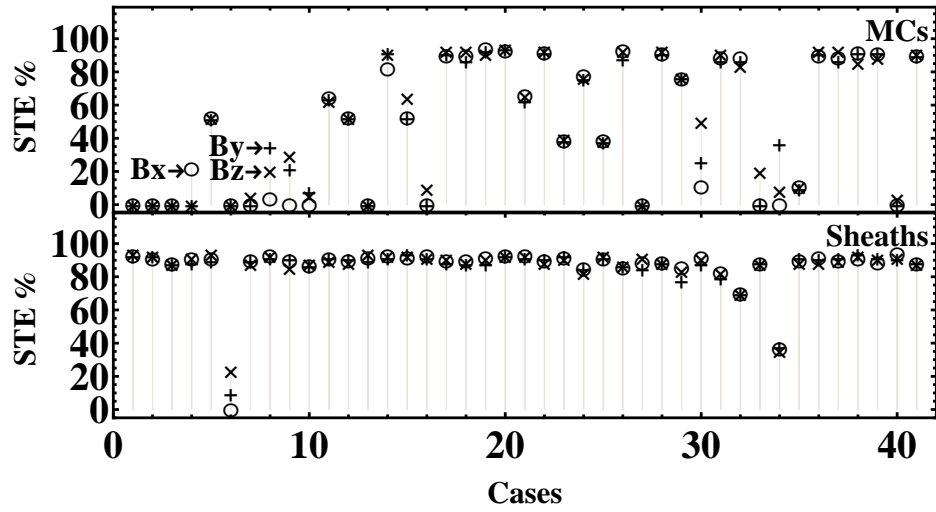


Figure 6. Format is the same as in Figure 4, but the trend was removed through the first-order differences at the time series.

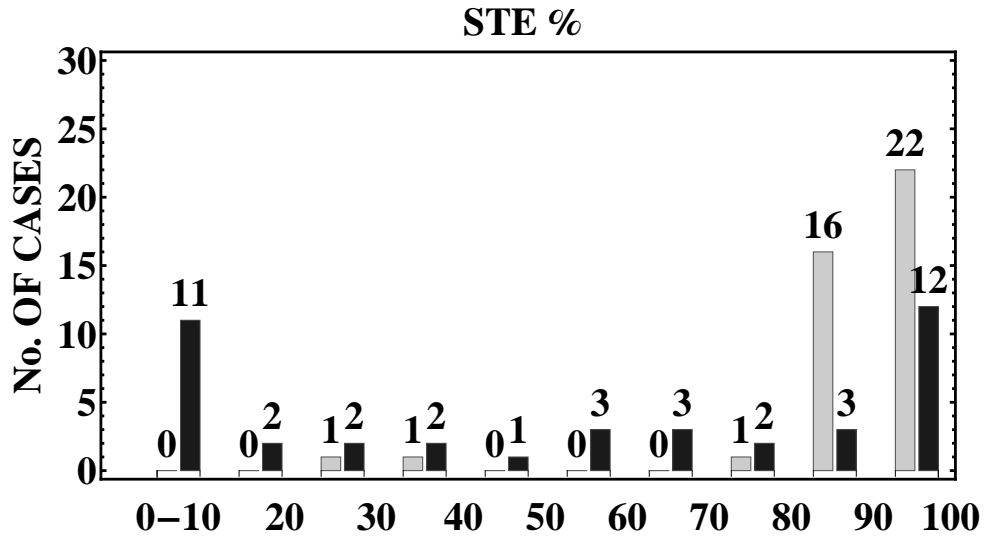


Figure 7. A histogram of STE derived from Figure 6 for B_z corresponding to MCs regions (in black) and plasma sheaths regions (in grey) respectively.

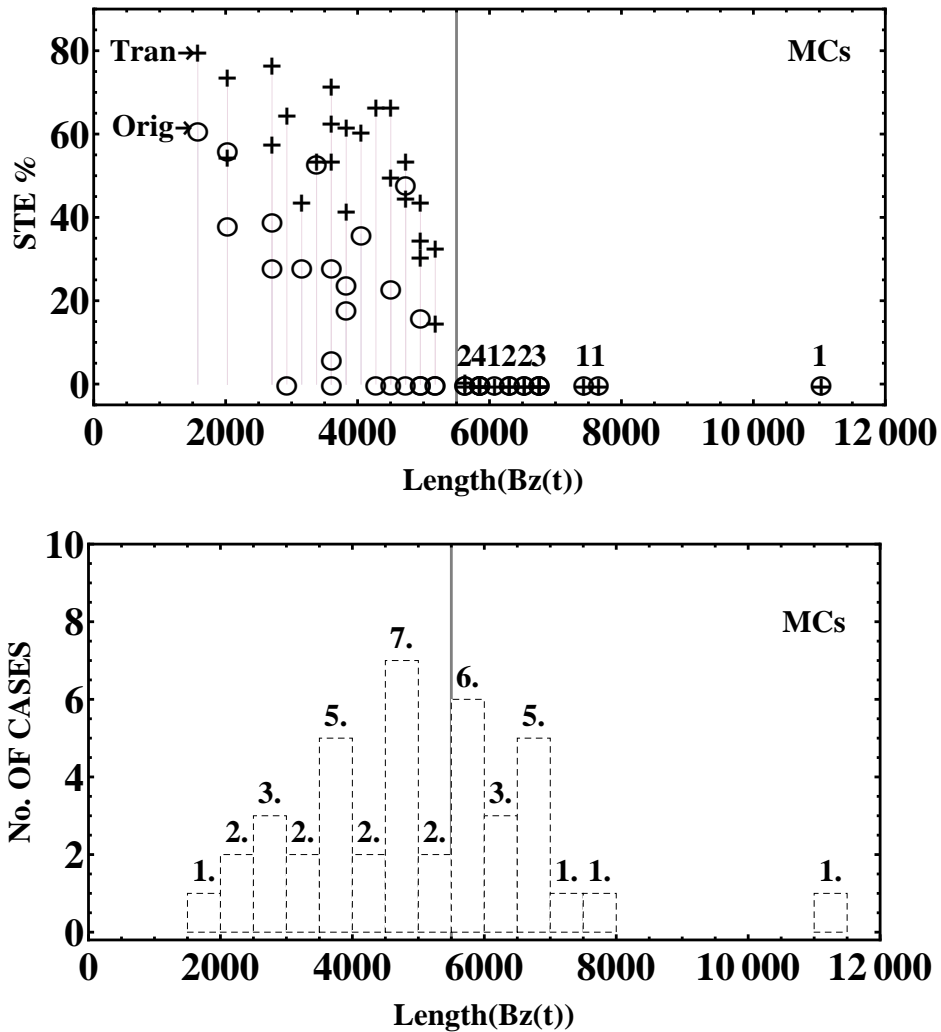


Figure 8. (top panel) STE values versus length of B_z time series using 41 MCs, where the “o” and “+” symbols corresponds to original and transformed (remove the Gaussian noise and trend through a rotation) time series respectively. To the right of the vertical line, larger clouds are shown, and by the software limitation the STE values are zero. (bottom panel) The histogram helps to identify overlapping points of MCs in the top panel.

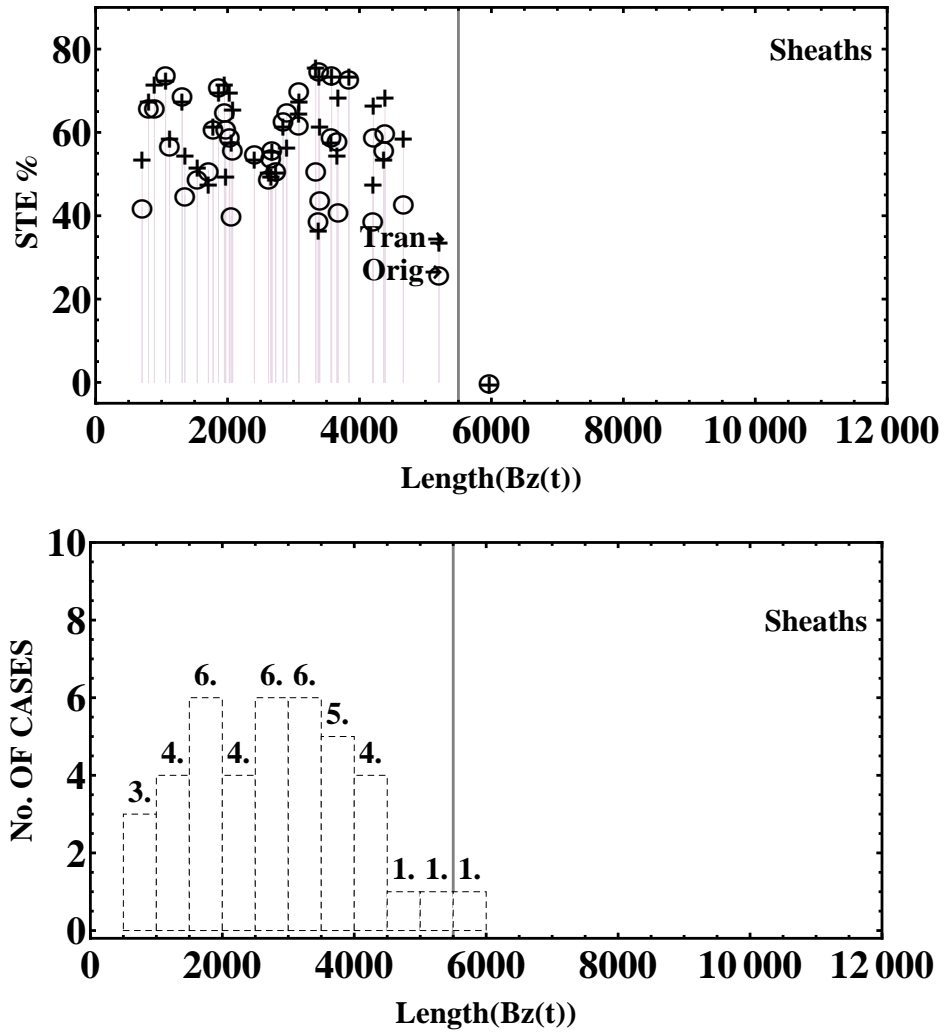


Figure 9. In both panels, the format is the same as in Figure 8, but STE values 41 plasma sheaths are plotted. (bottom panel) The histogram helps to identify overlapping points of sheaths in the top panel.

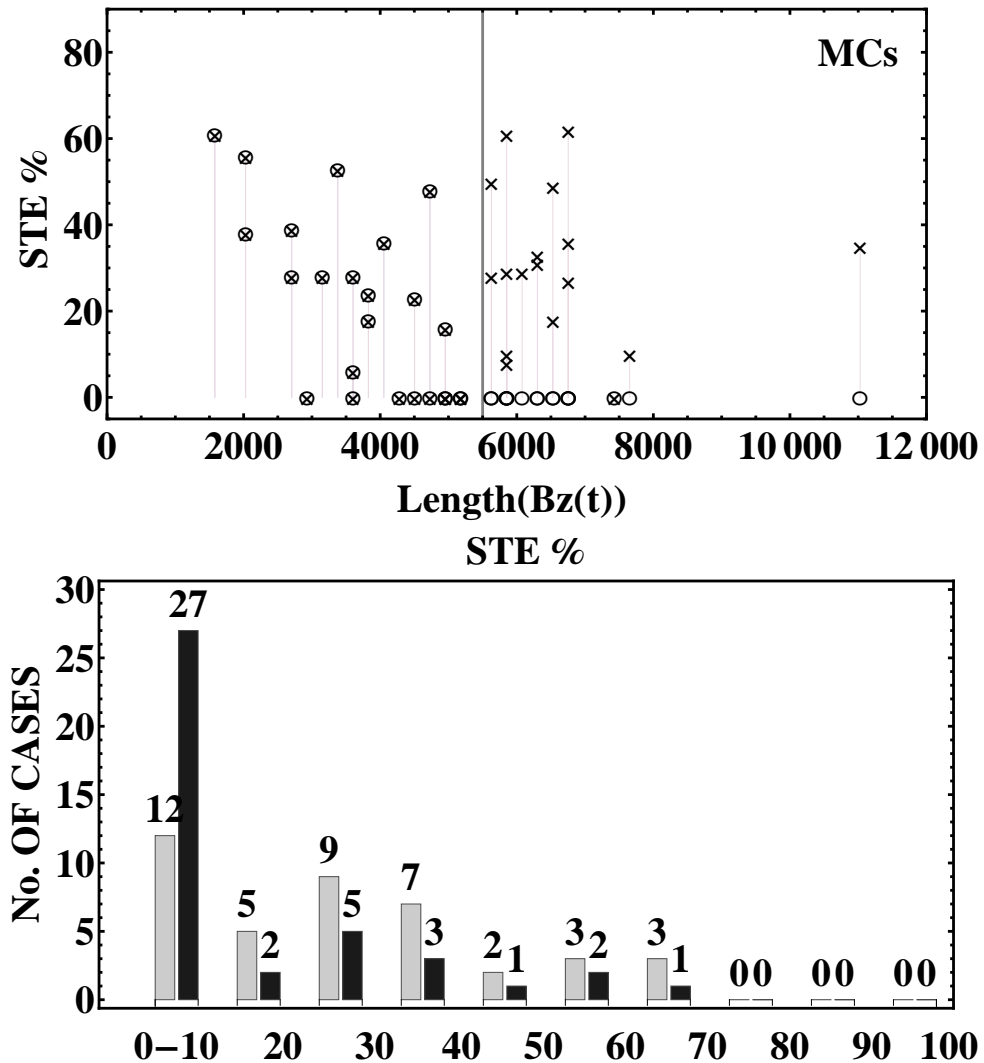


Figure 10. We selected MCs sample with less of 5500 points, taking the intervals between the positions 500 until 4500 in IMF B_z . (top panel) The “o” and “x” symbols correspond to non-transform and transformed (reduced to 4001 points) time series respectively. (bottom panel) A histogram of STE derived from top panel corresponding to transformed (in grey) and non-transform (in black) of B_z time series.

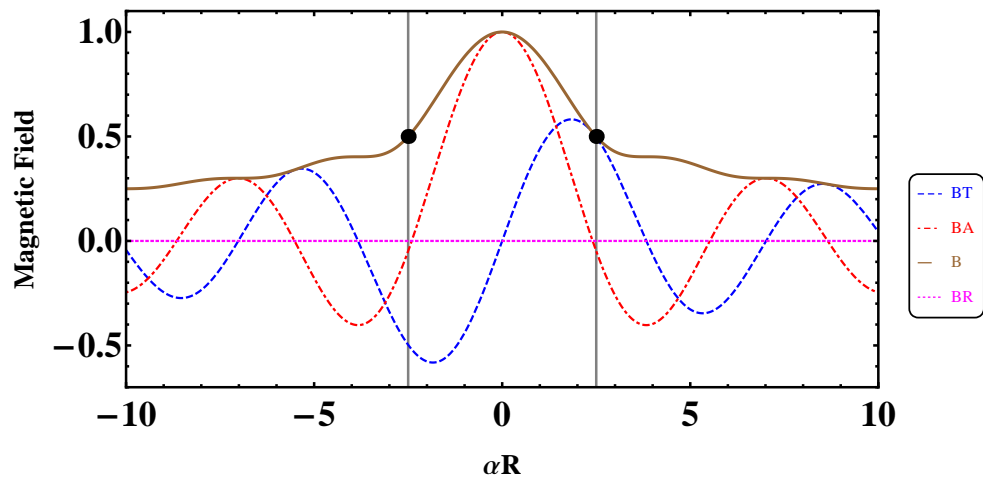


Figure 11. The force-free model solution (axial, tangential and radial components and total magnetic field) as solved in Burlaga [1988] were plotted. Following Burlaga [1988], we show the boundaries with two vertical lines at the points where $B_A = 0$, i.e. where $\alpha \cdot R = 2.4$ and $B/B_0 = 0.5$, also $\alpha = 1$.

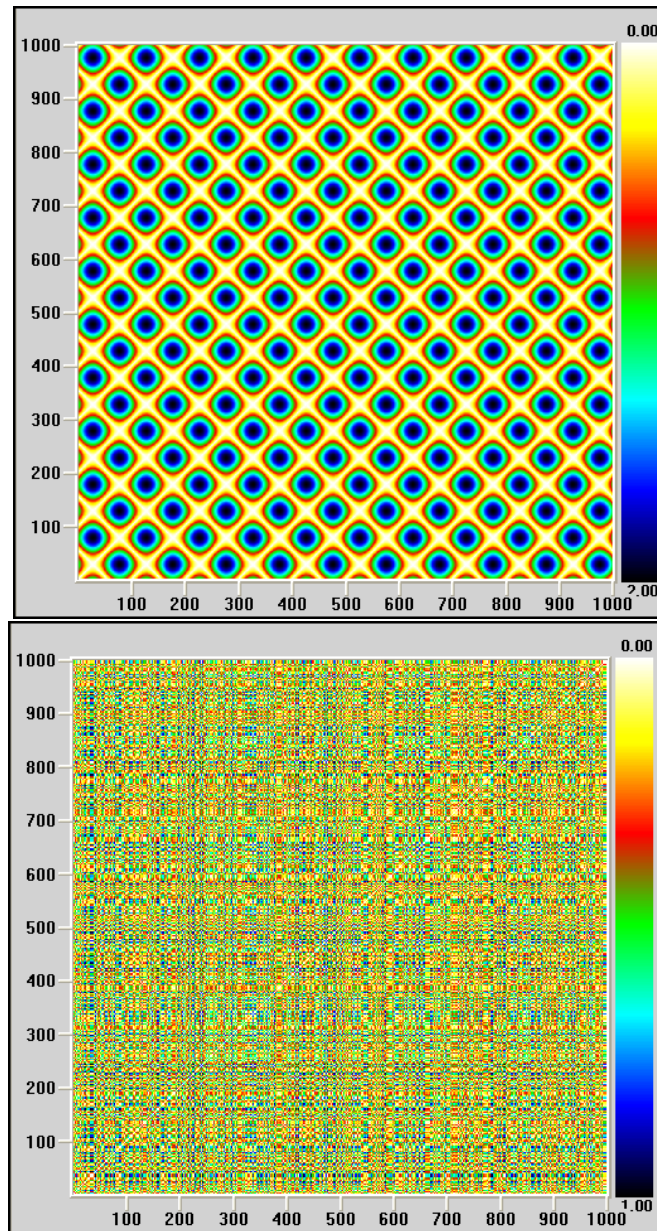


Figure 12. Recurrence plot using a data files included with VRA software. (top panel) In the RP organized patterns of color characteristics are shown for a periodic signal; sine wave with $STE = 0\%$. (bottom panel) In the RP an uniform distribution of color characteristics is shown for a random signal, white noise with $STE = 80\%$.

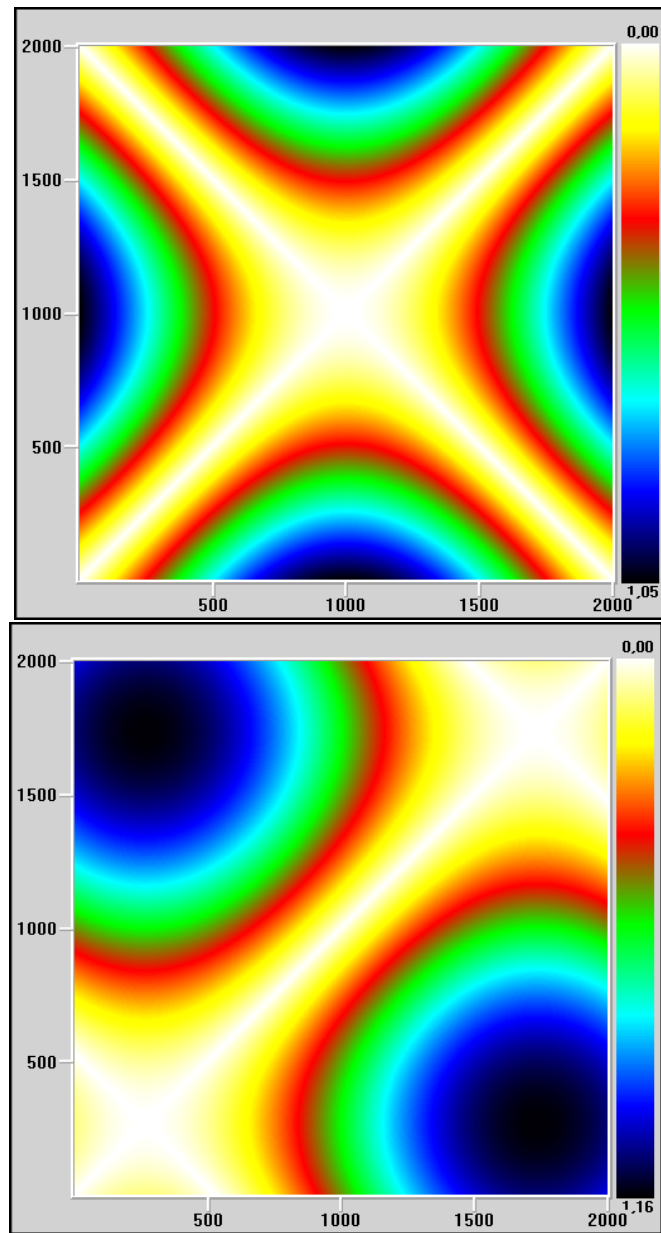


Figure 13. RPs of the solution for a cylindrically symmetric force-free field with constant alpha are shown. (top panel) Axial component : $B_A = B_0 J_0(\alpha R)$, $STE = 27\%$. (bottom panel) Tangential component : $B_T = B_0 H J_1(\alpha R)$, $STE = 0\%$.